Origin of spectral rogue waves in incoherent optical wave packets

Yueqing Du, Zhiwen He, Heze Zhang, Qun Gao, Chao Zeng, Dong Mao,[*] and Jianlin Zhao

Key Laboratory of Light Field Manipulation and Information Acquisition, Ministry of Industry and Information Technology,
School of Physical Science and Technology, Northwestern Polytechnical University, Xi'an 710129, China

The rogue wave (RW) is a persistent topic in diverse fields of science including optics, hydromechanics, and electromagnetics. Despite the extensive experimental confirmations, the optical RW in the spectral domain is still elusive in aspects of its origination and evolutionary dynamics. Operating the fiber laser in a noiselike pulse (NLP) state, we observe the spectral RW according to the statistics of the shot-to-shot spectral evolution. Simulations consistent with experiments reveal that the spectrograms of NLPs are constituted by multiple localized speckles in the temporal-spectral domain, which originate from the interferences in the temporal and spectral domains. The collective motion of speckles is dominated by the Kerr effect and group-velocity dispersion. Several speckles can be in alignment at the same frequency, promoting the generation of the spectral RW. This paper sparks interest in the physics of incoherent wave packets widely existing in nonlinear optical systems.

I. INTRODUCTION

The rogue wave (RW) is a ubiquitous phenomenon in various physical systems [1–3], referring to the enhancement of wave parameters, e.g., wave height or energy in an unpredictable, rare, and extreme manner [4–8]. Originally, the term RW was proposed to describe the freak waves with extreme heights in seas that are responsible for many oceanic disasters [9,10]. Now the contents of RW have been remarkably enriched in several regards: the underlying mechanisms of RWs can be linear [3,11,12] or nonlinear [13,14], the physical domains where a RW exists can be temporal [15,16], spectral [17,18], and spatial [14,19] ones, and systems wherein the RWs exist can be conservative [20] and dissipative [21]. Compared with fluid dynamic systems such as the ocean or water tanks [2,10,22], optical systems with a compact size are ideal testbeds for exploring the nonlinear physics of RWs in spatial and temporal domains [8], which have been observed in lasers [15,16,23], optical cavities [19], multimode fibers [11], and Kerr media [14]. Solli *et al.* [1] discovered temporal RWs based on the shot-to-shot statistics of the long-wavelength component in the supercontinuum. It has been recognized that collisions between solitons and breathers are responsible for the generation of temporal RWs in conservative optical systems [20,24–27]. In dissipative systems like lasers, temporal RWs are induced by pulse collision [21,28–30], wave amplification [31–33], and temporal focusing [34–36].

With the wide application of ultrafast spectroscopy like the dispersive Fourier transform (DFT) method [37], the transient spectral dynamics in lasers have attracted intense interest [37–39]. Subsequently, spectral RWs have been observed in incoherent wave packets such as the exploding soliton [17,40–42] and noiselike pulse (NLP) [18,43–45]. An incoherent wave packet such as a NLP is a cluster of temporal structures varying stochastically with time, whose interferences result in disordered spectral patterns, constituting a hotbed for the generation of the spectral RW. The nonlinearities, e.g., Kerr effect or Raman scattering, are the backbone, accounting for the collective kinetics of such spectral structures. In an intriguing case of a NLP, the sporadically emitted redshifted component induced by the Raman effects [18] is regarded as the spectral RW. Nonetheless, when the power of the wave packet is not strong enough to stimulate the Raman scattering, e.g., in cases of the conventional NLP [43,44], or exploding solitons [17,40–42], the spectral dynamics are dominated by the Kerr effect and dispersion, under which the universal mechanism responsible for the spectral RW is unclear.

In this paper, we explore the formation mechanism and dynamical properties of spectral RWs in NLP lasers. The NLP is a wave packet composed of multiple temporal structures, whose interference produces complex patterns in the spectral domain. In turn, the interference between spectral structures results in complex temporal structures. Such a two-dimensional interference gives rise to multiple localized speckles in the spectrogram of a NLP in the spectral-temporal domain, in analogy to the generation of spatial speckles [46,47]. The collective motion of multiple speckles within the NLP is determined by the composite effect of the Kerr nonlinearity and dispersion. During the stochastic evolution, several speckles at different temporal locations can shift to a certain frequency, at which the spectral structure is enhanced to be a RW. This paper is a step toward exploring the turbulent dynamics and mechanism of spectral RWs, which has potential in optical random bit generation [48], chaos communications [49], and supercontinuum generation [46].
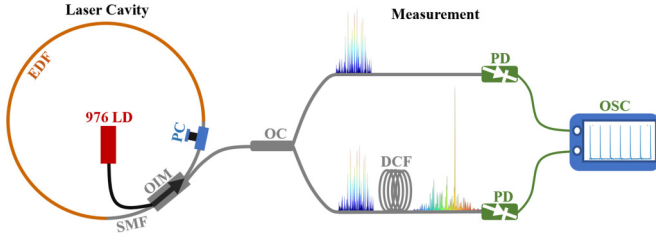
---

*maodong@nwpu.edu.cn

FIG. 1. Configurations of the laser cavity and real-time measurement setup of the noiselike pulse. EDF: erbium-doped fiber; SMF: single-mode fiber; LD: laser diode; OIM: optical integrated device, including a polarization-sensitive isolator, wavelength-division multiplexer, 30/70 output coupler; OC: output coupler; DCF: dispersion-compensation fiber; PD: photoelectric detector; and OSC: oscilloscope.

II. RESULTS

A. Spectral/temporal properties of the incoherent pulse

The fiber laser comprises a 10-m Er-doped fiber (EDF) and 5-m single-mode fiber (SMF) with a net-normal dispersion of ~ 0.09 ps^2. The partial mode locking with the threshold of 195 mW is achieved by the nonlinear polarization rotation (NPR) [50]. The details of the laser and measurement systems are described in Appendix A, and the corresponding schematic diagram is displayed in Fig. 1. Thanks to the strong nonlinearity of the long cavity and the nonmonotonic loss of NPR [50], we can achieve the robust NLP mode locking at the 330-mW pump power, as shown in Fig. 2. The average spectrum of the NLP sequence has a smooth profile with a
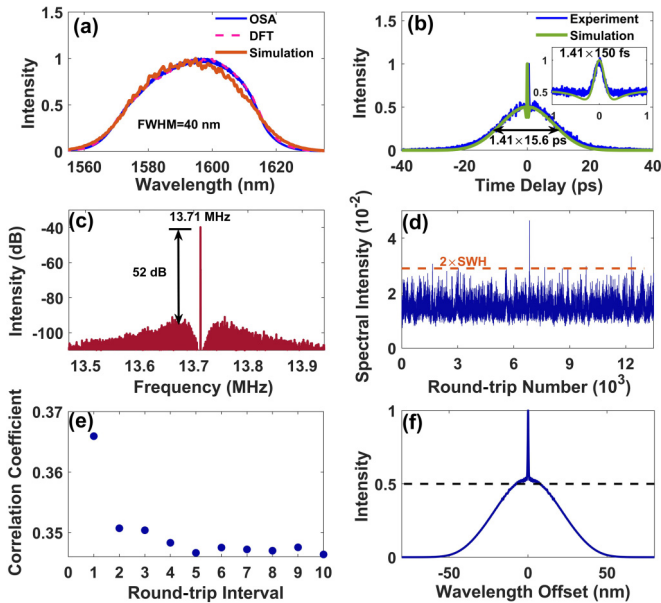

FIG. 2. Experimental and simulated results of the noiselike pulse associated with spectral rogue waves. (a) Spectrum. (b) Intensity autocorrelation trace (ACT). (c) Radiofrequency spectrum. (d) Spectral intensity evolution over 13 000 roundtrips (RTs). (e) Correlation coefficients between two single-shot spectra at different interval RTs, i.e., the interpulse coherence. (f) ACT of the single-shot spectrum averaged over 13 000 RTs, i.e., the intrapulse coherence.

full width at half maximum of 40 nm. The well-fitted spectra measured by the optical spectral analyzer and DFT indicate the accuracy of the DFT technique. The intensity autocorrelation trace (ACT) of the NLP is composed of a 150-fs coherent peak and a 15.6-ps incoherent pedestal [Fig. 2(b)], indicating the incoherence of temporal structures inside the wave packet. The simulated spectrum and intensity ACT agree well with experimental ones, confirming the reliability of the simulation model and parameters [details of simulations are described in Appendix B]. The gain filter in the simulation has a symmetric profile, while the actual gain profile of EDF is uneven in the experiment, which results in a slight difference between two spectral profiles.

The stability of the NLP is confirmed by the 52-dB signal-to-noise ratio at the fundamental repetition rate of the radiofrequency spectrum [Fig. 2(c)]. We capture the shot-to-shot spectral evolution using the DFT and then extract the peak intensity of each single-shot spectrum [Fig. 2(d)]. The significant wave height (SWH) is defined as the average value of the top third of the spectral intensities, while the pulse whose spectral intensity exceeds twice the SWH is regarded as a RW. From the spectral evolution in Fig. 2(d), one can see several spectral enhancement events that exceed the RW threshold.

The fast-varying spectral intensity vs roundtrips (RTs) implies the weak correlation between spectra at different RTs (interpulse coherence). We use the Pearson correlation coefficient [51] to quantify the interpulse coherence of the NLP, the details of which can be found in Appendix C. In short, the larger Pearson coefficient indicates a stronger linear correlation between two single-shot spectra and vice versa. As shown in Fig. 2(e), the correlation of the two spectra decreases monotonically with the increase of their RT interval and converges to ~ 0.35 when the RT interval is >6. A correlation <0.4 demonstrates the weak interpulse coherence. The tendency in Fig. 2(e) shows that a larger RT interval results in a weaker correlation between two spectra, i.e., the nonlinear evolution of the NLP weakens the correlation between two NLPs of different RTs.

Furthermore, the NLP is a bunch of weakly correlated temporal structures [Fig. 2(b)], whose interference can produce a bunch of spectral structures. Thus, it is natural that the correlation between spectral structures within one pulse (intrapulse coherence) is also weak, as demonstrated by the spectral ACT in Fig. 2(f), which is constituted by a broad pedestal and a narrow spike like the temporal ACT. The intensity of the pedestal is slightly >0.5, indicating the spectral structures are not completely irrelevant. This can be explained: The NLP is composed of many tiny pulses with femtosecond scales. For a certain tiny pulse, it has a broadband spectrum in the spectral domain; therefore, two spectral structures will share the same temporal tiny pulse, i.e., they are correlated to some extent. The results in Figs. 2(e) and 2(f) show that the NLP has interpulse and intrapulse incoherence, which means the emerged rogue structure is isolated in both the wavelength and RT directions, i.e., the feature of appearing from nowhere [24].

The evolution and statistics of the NLP associated with spectral RWs are displayed in Figs. 3(a)–3(c). In the spectral evolution [Fig. 3(a)], the RW manifests as a bright spot that
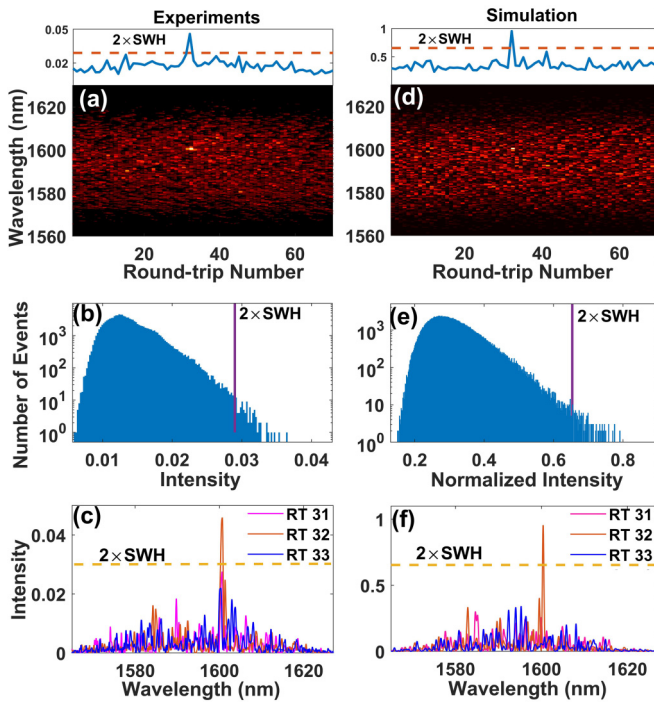
FIG. 3. Experimental (left column) and simulated (right column) results of the noiselike pulse associated with spectral rogue waves. (a) and (d) Spectral evolutions. (b) and (e) Histograms of spectral intensities. (c) and (f) Single-shot spectra of three consecutive roundtrips.
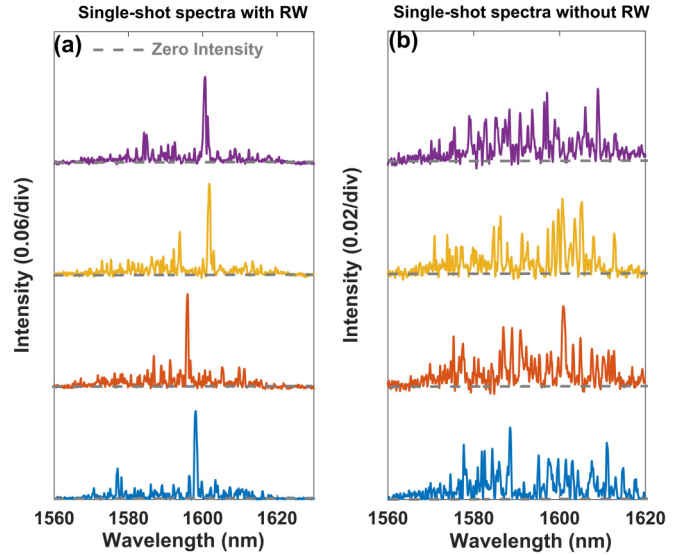

FIG. 4. (a) Experimentally captured four single-shot spectra whose intensities exceed the rogue wave (RW) threshold. (b) Four spectra without spectral RW.

is localized in both the RT and wavelength directions, arising from the intrapulse and interpulse incoherence of the NLP. Statistics of spectral intensities over 60 000 RTs [Fig. 3(b)] feature a long-tailed probability distribution like the temporal RW in chaotic pulse bunches [21], whose large intensity side exceeds the RW threshold. Three spectra at consecutive RTs [Fig. 3(c)] contain many fine structures arising from the interference between temporal structures. One of the spectral structures at the 32nd RT exceeds the RW threshold, manifesting as the transient spectral enhancement in the shot-to-shot intensity evolution [upper panel of Fig. 3(a)]. Simulation results in Figs. 3(d)–3(f) agree qualitatively well with experimental results, demonstrating that the NLP and spectral RW can be well reproduced by the simulation based on the generalized nonlinear Schrödinger equation and the ring cavity model. Details of the simulation are given in Appendix B. Based on the analysis of several RW events in experiments [see Fig. 4], we can conclude that only one spectral structure can be enhanced to be a spectral RW rather than the overall enhancement of the spectral wave packet, implying that the spectral enhancement originates from the interactions between fine structures instead of the gain dynamics that can be shared by every spectral structure. The mechanism of the local spectral enhancement will be discussed in the following section.

B. Intracavity evolution of NLP

The good agreement between simulation and experiment ensures the reliability of our further exploration of the spectral

RW based on the simulation. We select one of the RWs in the simulation to investigate its intracavity evolution [Fig. 5], wherein the spectral RW emerges at the second RT. The spectral fine structures randomly increase and decay in the cavity [Fig. 5(a)], and one of them exceeds the RW threshold at the output coupler (OC) at the second RT [Fig. 5(a₂)]. We find that the spectral peak that evolves into a RW at the OC corresponds
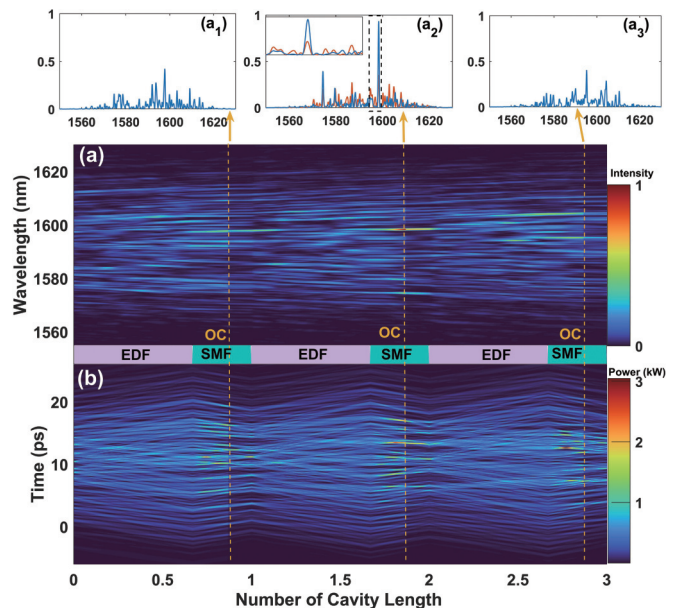

FIG. 5. Simulated intracavity evolution of noiselike pulse over three roundtrips (RTs, 68 661–68 663), during which the spectral rogue wave appears at the output coupler (OC) in the second RT. (a) Spectral evolution. (b) Temporal evolution. (a1)–(a3) Single-shot spectra at the OC of three RTs. In (a2), the orange solid curve is the spectrum at the beginning of single-mode fiber (SMF), while the blue solid curve corresponds to the spectrum at the OC.
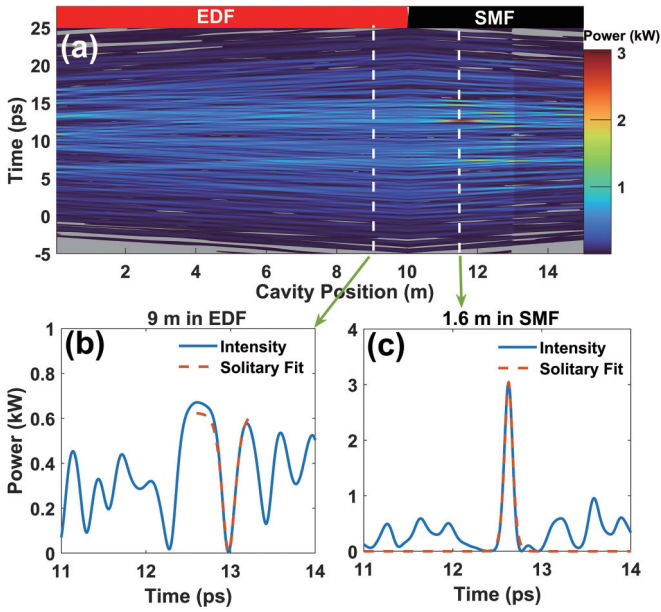
FIG. 6. Simulated dark and bright solitons in the normal and anomalous dispersion region of the cavity. (a) Intracavity temporal evolution. (b) Intensity profile and its solitary fit of the dark soliton at the marked position. (c) Intensity profile and its solitary fit of the bright soliton at the marked position.

to the strongest spectral peak at the end of the EDF [inset of Fig. 5(a₂)], which is universal for all cases of spectral RWs. This is natural that the strongest spectral peak amplified by the EDF has the most probability to evolve into a RW at the OC. In addition, it is the stochastic intracavity evolution that facilitates the weak correlation between the NLPs of two RTs [Figs. 5(a₁)–5(a₃)].

In the temporal domain [Fig. 5(b)], the wave packet experiences periodic broadening and narrowing governed by the dispersion management of the cavity (normal dispersion in the EDF and anomalous dispersion in SMF). In contrast to the evolution of the wave packet, the inner structures evolve turbulently due to the composite effect of dispersion, nonlinearity, and interactions between temporal structures. In the normal-dispersion EDF, one can see the traces of dark pulses, while the waves gradually evolve into bright pulses in the anomalous-dispersion SMF [see Fig. 6]. The spontaneous emergence of solitary structures (both dark and bright) is caused by self-organization in the presence of the dispersion and nonlinearity [52,53].

It is difficult to ascertain the mechanism of the spectral RW based on the individual spectral or temporal evolutions. Considering the strong relevance between the temporal and spectral properties of the wave packet, we calculate the spectrograms of NLPs via the short-time Fourier transform, as displayed in Fig. 7. The overall wave packet presents the up-chirp caused by the composite effects of net-normal dispersion and Kerr nonlinearity. There are multiple speckles in the spectrogram induced by the temporal and spectral interferences. When several strong speckles locate at different frequencies, the NLP at RT 68 662 has no RW in the spectral domain [Fig. 7(a)]. In the next RT [Fig. 7(b)], when three strong speckles at different temporal locations appear
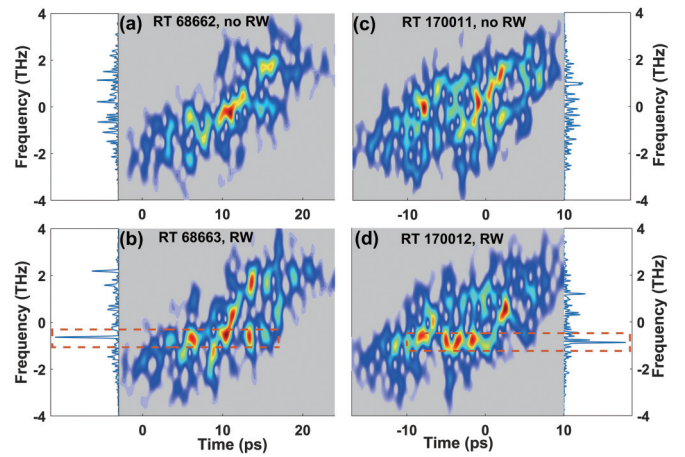

FIG. 7. Simulated spectrograms of noiselike pulses (a) and (c) with and (b) and (d) without rogue waves.

in the vicinity of ∼−0.63 THz, the spectral RW emerges in the spectral domain at this frequency [left panel of Fig. 7(b)]. We found that all the RWs are induced by the alignment of several speckles (at different temporal locations) in the vicinity of a certain frequency, as corroborated by another example in Figs. 7(c) and 7(d); thus, the spectral RW in the experiment and simulation manifests as the local enhancement of one spectral peak rather than the overall enhancement of all spectral structures.

C. Internal motion dynamics and mechanisms of NLP

It is significant to understand the collective motion dynamics and mechanisms of multiple speckles within the NLP, which dominate the formation and decaying of the spectral RW. In this section, we take the spectral RW in RT 68 663 as an example to reveal how the Kerr effect and dispersion dominate the collective motion of speckles. After propagating 2 m in the SMF [Fig. 8(a)], two speckles marked by SP1 and
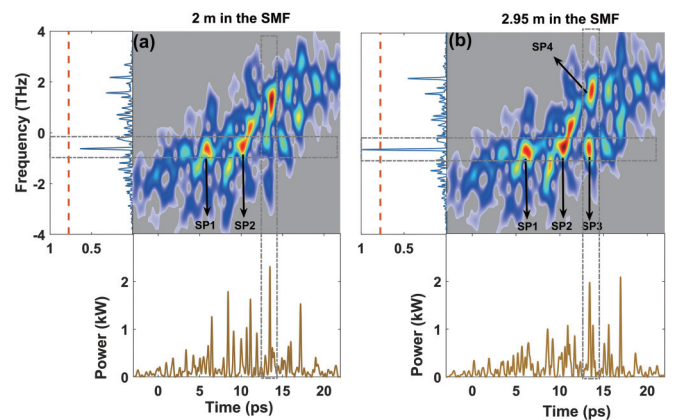

FIG. 8. Simulated spectrograms of the noiselike pulses at the cavity positions of (a) 2 m and (b) 2.95 m in the single-mode fiber. At ∼−0.63 THz, the spectrogram has two speckles (SP1 and SP2) in (a) and three speckles (SP1, SP2, and SP3) in (b), respectively. The bottom and left panels are the spectral and temporal profiles, respectively.
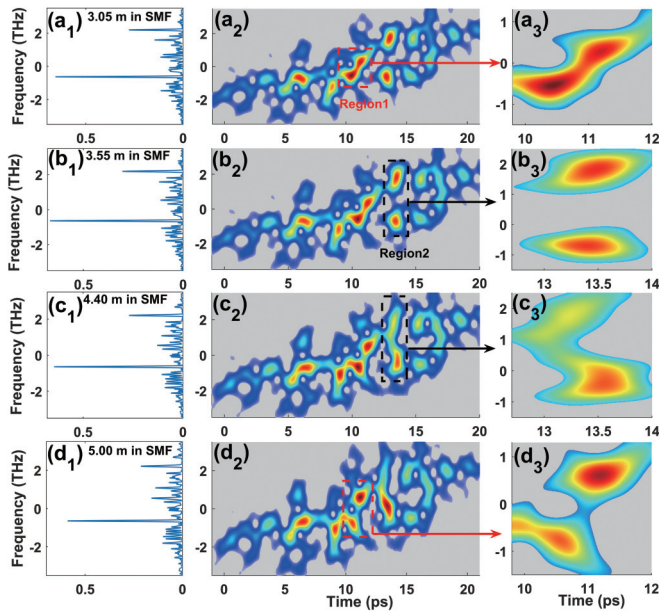
FIG. 9. Simulated degradation of the spectral rogue wave in the single-mode fiber. The first column: spectra of the noiselike pulse at different cavity positions. The second column: spectrograms at different cavity positions. The third column: enlarged visualization of the marked region in the spectrogram. The two speckles in Region 1 repel each other, while the two speckles in Region 2 attract each other.
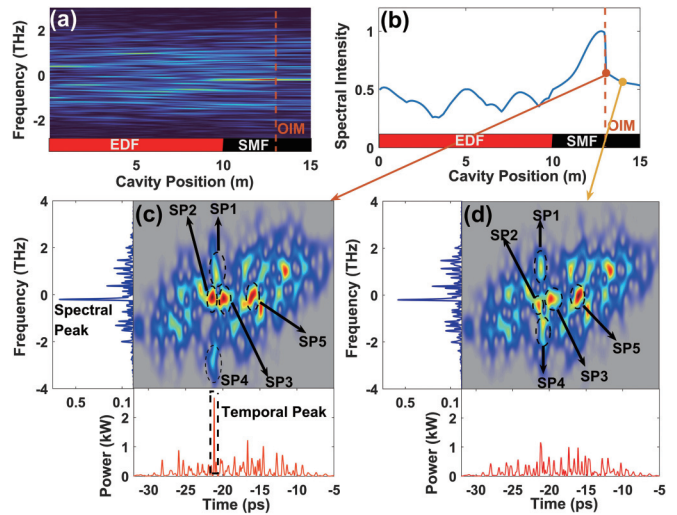

FIG. 10. Simulated results of the noiselike pulse evolution when the spectral rogue wave emerges at the output coupler. All the parameters in the simulation are the same as those of the simulation in this paper. (a) Intracavity spectral evolution. (b) Intracavity spectral intensity evolution. (c) Spectrogram of the wave packet at the cavity position of 13.05 m. (d) Spectrogram of the wave packet at the cavity position of 14. Left panels of (c) and (d) are the corresponding spectra, while the bottom panels are the temporal intensity profiles.

SP2 locate at ∼−0.63 THz, forming a strong spectral peak lower than the RW threshold. At the same time, a strong temporal pulse [lower panel of Fig. 8(a)] at ∼13 ps corresponds to a speckle in the spectrogram. After the 0.95-m propagation in SMF [Fig. 8(b)], the temporal pulse at 13 ps experiences SPM-induced spectral splitting as well as the cross-phase-modulation (XPM) by the adjacent pulses, generating two speckles marked as SP4 and SP3 moving toward the high- and low-frequency sides, respectively. When SP3 reaches ∼−0.63 THz, the interference between SP1, SP2, and SP3 gives rise to the spectral peak that exceeds the RW threshold.

Due to the interactions between speckles in the NLP mediated by the Kerr effect and dispersion, the spectral RW is unstable and decays during subsequent propagation in the cavity, as depicted in Fig. 9. Two local regions in the spectrogram are marked as regions 1 and 2, wherein the exemplary motions of speckles are useful to understand the decaying of spectral RW.

In Region 1, the distribution of two speckles takes the form of an up-chirp state, so the high-frequency speckle imposes the redshift on the low-frequency speckle via XPM [54], and in turn, the low-frequency speckle can induce the blueshift to the high-frequency component. Consequently, two speckles in Region 1 will repel each other along the spectral direction, as one can get from Figs. 9(a)–9(d).

In Region 2, the distributions of two speckles present chirp-free states [Fig. 9(b₂)]. Ascribing to the anomalous dispersion, the high-frequency component moves in front of the low-frequency component in the temporal domain [Figs. 9(b) and 9(c)]. The temporal tail of high-frequency speckle gives rise to the blueshift of the low-frequency speckle, and in-

versely, the temporal head of low-frequency speckle induces the redshift of the high-frequency speckle. As a result, two speckles in Region 2 attract each other and finally merge into one speckle, i.e., the spectral narrowing. Note that this scenario is inspiring to understand the spectral narrowing of a down-chirped pulse in the SMF [55,56], and the initial spectral narrowing of a high-order soliton [54]. The visualization of the evolution of spectrogram in the SMF can be seen in Movie 1 in the Supplemental Material [57].

Note that the two low-frequency speckles in regions 1 and 2 both contribute to the spectral RW. After propagating in the SMF [Figs. 9(a)–9(d)], the two low-frequency speckles deviate from ∼−0.63 THz due to the complex motions described above. Therefore, the spectral peak at −0.63 THz weakens in the SMF and finally disappears in the EDF of the next RT. In addition to the paradigm discussed in this section, we show another paradigm of the decaying process of the spectral RW [see Fig. 10], further elucidating the dominance of the Kerr effect and dispersion. Simulation results demonstrate that the specific motion dynamics of the spectral RW might be distinct in different RW events; however, the governing mechanism is simple and universal.

From the above analysis, we can get that the formation of the spectral RW requires the alignment of several speckles to a certain frequency, and additionally, such an event should happen at the cavity position of the OC (the measurement and statistics are carried out at this position). Thus, the stochastic collective motion of multiple speckles, combined with the stringent requirements for the cavity position of the event, makes the extreme spectral enhancement captured at the OC very rare. When several speckles reach the alignment, such a state cannot sustain for a long time due to interactions between

speckles; therefore, the formed spectral RW will annihilate quickly.

III. DISCUSSION

We have completed the full description of the formation and decaying of the spectral RW based on the motion dynamics of pivotal speckles in the NLP. Several universal discussions and conclusions are necessary to understand the spectral turbulence of such an incoherent wave packet. For each speckle, it can be distorted by the interplay between dispersion and the Kerr effect. Its temporal motion is determined by the frequency and dispersion, while the spectral motion depends on the SPM and the XPM by its adjacent speckles. The collective motion of the speckles in the NLP is determined by the composite effect of dispersion and the Kerr nonlinearity. In addition to the scope of spectral RWs in this paper, the above discussions are useful for understanding the transient dynamics of spectral narrowing [56], high-order soliton [54], birefringence-managed soliton [58], and multicolor solitons [59,60].

In this paper, we focus on the intrapulse motion dynamics of the NLP, while notable work has demonstrated that interpulse interactions can also introduce the spectral RW. For example, when there are two pulses in the cavity, their periodic collision can generate the spectral RW [41]. The radiation of the ultrashort pulse laser contains various components, e.g., the soliton, polarized components, dispersive waves, and continuous waves, so whether the interactions between different components can generate spectral RWs and the accompanied intriguing phenomena are worth exploring.

IV. CONCLUSIONS

In conclusion, we reveal the formation and evolution of the spectral RW in the incoherent wave packet from an ultrashort pulse laser. Temporal and spectral interferences between fine structures result in multiple speckles in the spectrogram of the NLP. The spectral RW is validated to originate from the collective motion of multiple speckles governed by the Kerr effect and dispersion. When several speckles move to the same frequency, their interference and superposition produce a local spectral peak exceeding the RW threshold. The stochastic interactions between speckles make the spectral RW feature rare, extreme, and unpredictable. The results pave an avenue to understanding the physical mechanism of spectral RWs, spectral kinetics of incoherent wave packets, and spectral turbulence in dissipative systems, which have potential in the spectral engineering of ultrashort pulses and supercontinuum seeded by the NLP.

APPENDIX A: LASER AND MEASUREMENT CONFIGURATIONS

The fiber laser has a ring cavity comprised of 10-m EDF (Nufern, EDFL 980 HP) and 5-m SMF (including pigtails of optical devices). To simplify the cavity and enhance the stability of mode locking, we use the optical integrated device (OIM) possessing versatile functions including the wavelength division multiplexer (980/1550), polarization-sensitive isolator, and OC (30/70). The cavity is pumped by a 976-nm laser diode (LD) in conjunction with the OIM. By properly setting the polarization controller (PC), the nonlinear polarization rotation can be realized due to the polarization-sensitive OIM.

Here, 30% of the lasing light is extracted outside the cavity for measurement. The pulse train is divided into two branches by an OC (20/80). One branch is detected by the photoelectric detector (PD, Thorlabs DET08CFC) without the time stretch. The other branch is dispersed by a 5-km dispersion-compensation fiber (DCF, 150 ps/nm/km at 1550 nm), then detected by the PD. In this way, the single-shot spectrum of each NLP can be measured according to the DFT theory [37]. Signals of two branches are simultaneously recorded by a 4-GHz oscilloscope (LeCroy, 740Zi-A). Thus, the resolution of the DFT is ∼0.33 nm.

APPENDIX B: SIMULATION MODEL

The generalized nonlinear Schrödinger equation is used to model the evolution of NLP inside the cavity, which includes the group velocity dispersion, Kerr nonlinearity, gain dispersion, and saturable absorption:

$$u_z = -\frac{i\beta_2 u_{tt}}{2} + i\gamma|u|^2 u + \frac{gu}{2} + \frac{gu_{tt}}{(2\Omega^2)}. \quad \text{(B1)}$$

The variables z, t, and u correspond to the propagate coordinate, the pulse local time, and the slow varying wave packet respectively. Here, β_2 is the second-order dispersion coefficient, γ is the Kerr nonlinearity of the fiber, and Ω corresponds to the gain bandwidth of the EDF (30 nm). Also, $g = g_0 \exp(-E_p/E_s)$ is the saturated gain of EDF, where g_0, E_p, and E_s are the small-signal gain coefficient, pulse energy in the time window, and gain saturation energy, respectively. For SMF, $g_0 = 0$, $\beta_2 = -22.8$ ps²/km, $\gamma = 1.3$ kW^{-1} m^{-1}. For EDF, $g_0 = 0.7$ m^{-1}, $E_s = 1900$ pJ, $\beta_2 = 20.8$ ps²/km, $\gamma = 4.2$ kW^{-1} m^{-1}. Starting from an incoherent pulse, the simulation is carried out via the symmetric split-step Fourier method.

The amplitude transmission function of the saturable absorber is $T = 1 - T_0/(1 + P/P_{sat})$, where T_0 is the modulation depth (70%), P is the instantaneous pulse power, and P_{sat} is the saturable power (30 W). We do not use the nonmonotonic model of the saturable absorber for simplicity, considering the model is enough to reproduce both the dynamical and statistical features of the NLP with spectral RWs.

APPENDIX C: STATISTICAL DETAILS

We measured the spectral correlation between different turns of the NLP, i.e., the interpulse correlation, by means of the Pearson correlation coefficient. Specifically, we calculated

the correlation for a spectrum $S(\lambda, z)$ at the RT of z and the spectrum $S(\lambda, z + k)$ at the RT of $z + k$ and then averaged the correlation coefficients obtained for the measured spectra at different RTs, which can be expressed as

$$C_{\text{inter}}(k) = \sum_{z=1}^{N-k} \frac{\text{cov}[S(\lambda, z), S(\lambda, z)]}{\sigma[S(\lambda, z)]\sigma[S(\lambda, z+k)]} \bigg/ (N-k), \quad \text{(C1)}$$

where C_{inter} is the average correlation coefficient between two single-shot spectra with an interval of k RTs. Here, cov and σ refer to the operations of covariance and standard deviation, respectively. Also, N is the total number of measured spectra in the pulse train.

To measure the correlation between the fine structures within the spectra, i.e., the intrapulse correlation, we calculate the autocorrelation of the single-shot spectrum at each RT and then average all the obtained ACTs along the z axis, which is calculated as

$$C_{\text{intra}}(\lambda) = \sum_{z=1}^{N} \frac{\int_{\lambda_1}^{\lambda_2} S(\lambda, z)S(\lambda + \Lambda, z)d\Lambda}{\lambda_2 - \lambda_1} \bigg/ N, \quad \text{(C2)}$$

where C_{intra} is the average value of all the spectral ACTs. Here, (λ_1, λ_2) is the wavelength interval of the measured spectrum. Also, N is the total number of single-shot spectra in the pulse train.

APPENDIX D: LOCAL ENHANCEMENT OF THE SPECTRAL RWs

Figure 4 shows four single-shot spectra of the RW events in the experiment. For all cases of spectral RWs [Fig. 4(a)], only one of the spectral structures exceeds the RW threshold rather than the enhancement of the whole spectrum. The spectrum without the spectral RW [Fig. 4(b)] is a cluster of fine structures, none of which is locally enhanced. Note that the scales of the y axes in Figs. 4(a) and 4(b) are different to clearly highlight the features of the two kinds of spectra. Such a phenomenon indicates that the spectral RW is not induced by the transient enhancement of the slow gain [61]. Therefore, the local enhancement of the spectrum is dominated by the internal motion dynamics of the fine structures as elucidated in this paper.

APPENDIX E: DARK AND BRIGHT SOLITONS IN THE WAVE PACKET

We find that the NLP spontaneously generates dark solitary structures when transmitted in normal-dispersion fiber, while bright solitary structures are generated in anomalous-dispersion fiber, as shown in Fig. 6. By carefully analyzing the shapes of these structures [Figs. 6(b) and 6(c)], the dark and bright pulses can be well fitted by the $\tanh^2$ and sech^2 profiles, respectively. Furthermore, the soliton orders of the dark and

bright pulses are calculated to be 1.13 and 0.83, respectively, which suggests the pulses are close to the fundamental dark or bright soliton. Such quasisolitary pulses are caused by the interplay between dispersion and Kerr nonlinearity. Of course, the pulses cannot evolve into a perfect soliton due to the stochastic interactions with other components inside the wave packet. This phenomenon was also confirmed in our previous works [34], indicating the connection between the incoherent wave packet and coherent solitary structures.

APPENDIX F: INTERNAL MOTION DYNAMICS OF THE SPECTRAL RW

Here, another spectral RW different from that in this paper is analyzed to enhance the understanding of how the Kerr effect and dispersion dominate the internal motion of the NLP. The parameters of the simulation are the same as those in the case of this paper.

In Fig. 10, one can see the amplification and decay of the spectral RW in the cavity. The corresponding spectral intensity vs position is shown in Fig. 10(b). After the OIM, the spectral intensity decreases in the rest segment of SMF. NLPs at the two marked positions of Fig. 10(b) are displayed in Figs. 10(c) and 10(d).

The spectrogram of the NLP has many localized speckles [Fig. 10(c)], among which we mark five speckles as SP1–SP5. Note that SP2, SP3, and SP5 locate at -0.2 THz, which facilitates a strong spectral peak at this frequency [right panel of Fig. 10(c)]. SP1 and SP4 originate from the SPM-induced spectral broadening of a strong temporal pulse [the down panel of Fig. 10(c)]. Thus, the basic scenario now is that SP2 and SP3 are at the leading and trailing edges of a strong temporal pulse constituted by SP1 and SP4, respectively.

After propagating ~ 0.9 m in the SMF [Fig. 10(c)], SP2 and SP3 experience redshift and blueshift due to the XPM from the temporal pulse [54], respectively. Such a frequency shift results in the decrease of the spectral peak at ~ -0.2 THz, i.e., the decay of the spectral RW. Additionally, under the anomalous dispersion, SP1 moves forward in the temporal direction, while SP4 moves backward, which gives rise to the temporal broadening and weakening of the pulse. When SP1 and SP2 are in front of SP3, and SP4 is behind SP3, the collective interactions between four speckles introduce the blueshift of SP4 because the blueshift induced by SP1 and SP2 is stronger than the redshift by SP3.

From this specific example, one can further understand the internal motion dynamics governed by the Kerr effect and dispersion. The enhancement and decay of the spectral RW depend on the motions of multiple speckles along the frequency direction, which is at the root of the XPM between speckles. However, the exact effect of the XPM on one certain speckle is sensitive to the relative temporal location between speckles. In other words, the dispersion also has a significant effect on the frequency shift of the speckle.

[1] D. R. Solli, C. Ropers, P. Koonath, and B. Jalali, Nature (London) **450**, 1054 (2007).

[2] M. Onorato, A. R. Osborne, M. Serio, and S. Bertone, Phys. Rev. Lett. **86**, 5831 (2001).

[3] R. Hohmann, U. Kuhl, H. J. Stockmann, L. Kaplan, and E. J. Heller, Phys. Rev. Lett. **104**, 093901 (2010).

[4] J. M. Dudley, G. Genty, A. Mussot, A. Chabchoub, and F. Dias, Nat. Rev. Phys. **1**, 675 (2019).

[5] J. M. Dudley, F. Dias, M. Erkintalo, and G. Genty, Nat. Photonics **8**, 755 (2014).

[6] N. Akhmediev, B. Kibler, F. Baronio, M. Belić, W.-P. Zhong, Y. Zhang, W. Chang, J. M. Soto-Crespo, P. Vouzas, P. Grelu *et al.*, J. Opt. **18**, 063001 (2016).

[7] Y. Song, Z. Wang, C. Wang, K. Panajotov, and H. Zhang, Adv. Photonics **2**, 024001 (2020).

[8] M. Tlidi and M. Taki, Adv. Opt. Photonics **14**, 87 (2022).

[9] T. A. Adcock and P. H. Taylor, Rep. Prog. Phys. **77**, 105901 (2014).

[10] A. Chabchoub, Phys. Rev. Lett. **117**, 144103 (2016).

[11] F. T. Arecchi, U. Bortolozzo, A. Montina, and S. Residori, Phys. Rev. Lett. **106**, 153901 (2011).

[12] C. Bonatto, S. D. Prado, F. L. Metz, J. R. Schoffen, R. R. B. Correia, and J. M. Hickmann, Phys. Rev. E **102**, 052219 (2020).

[13] A. Safari, R. Fickler, M. J. Padgett, and R. W. Boyd, Phys. Rev. Lett. **119**, 203901 (2017).

[14] S. Birkholz, E. T. Nibbering, C. Bree, S. Skupin, A. Demircan, G. Genty, and G. Steinmeyer, Phys. Rev. Lett. **111**, 243903 (2013).

[15] A. N. Pisarchik, R. Jaimes-Reategui, R. Sevilla-Escoboza, G. Huerta-Cuellar, and M. Taki, Phys. Rev. Lett. **107**, 274101 (2011).

[16] C. Bonatto, M. Feyereisen, S. Barland, M. Giudici, C. Masoller, J. R. Leite, and J. R. Tredicce, Phys. Rev. Lett. **107**, 053901 (2011).

[17] M. Liu, A. P. Luo, W. C. Xu, and Z. C. Luo, Opt. Lett. **41**, 3912 (2016).

[18] A. F. Runge, C. Aguergaray, N. G. Broderick, and M. Erkintalo, Opt. Lett. **39**, 319 (2014).

[19] A. Montina, U. Bortolozzo, S. Residori, and F. T. Arecchi, Phys. Rev. Lett. **103**, 173901 (2009).

[20] P. Suret, R. E. Koussaifi, A. Tikan, C. Evain, S. Randoux, C. Szwaj, and S. Bielawski, Nat. Commun. **7**, 13136 (2016).

[21] C. Lecaplain, P. Grelu, J. M. Soto-Crespo, and N. Akhmediev, Phys. Rev. Lett. **108**, 233901 (2012).

[22] A. Toffoli, T. Waseda, H. Houtani, T. Kinoshita, K. Collins, D. Proment, and M. Onorato, Phys. Rev. E **87**, 051201 (2013).

[23] F. Selmi, S. Coulibaly, Z. Loghmari, I. Sagnes, G. Beaudoin, M. G. Clerc, and S. Barbay, Phys. Rev. Lett. **116**, 013901 (2016).

[24] N. Akhmediev, J. M. Soto-Crespo, and A. Ankiewicz, Phys. Rev. A **80**, 043818 (2009).

[25] N. Akhmediev, J. M. Soto-Crespo and A. Ankiewicz, Phys. Lett. A **373**, 2137 (2009).

[26] J. M. Soto-Crespo, N. Devine, and N. Akhmediev, Phys. Rev. Lett. **116**, 103901 (2016).

[27] S. Toenger, T. Godin, C. Billet, F. Dias, M. Erkintalo, G. Genty, and J. M. Dudley, Sci. Rep. **5**, 10380 (2015).

[28] J. Peng, N. Tarasov, S. Sugavanam, and D. Churkin, Opt. Express **24**, 21256 (2016).

[29] J. M. Soto-Crespo, P. Grelu, and N. Akhmediev, Phys. Rev. E **84**, 016604 (2011).

[30] J. Liu, X. Li, S. Zhang, L. Liu, D. Yan, and C. Wang, Opt. Express **29**, 30494 (2021).

[31] S. Lee, K. Park, H. Kim, L. A. Vazquez-Zuniga, J. Kim, and Y. Jeong, Opt. Express **26**, 11447 (2018).

[32] A. Klein, G. Masri, H. Duadi, K. Sulimany, O. Lib, H. Steinberg, S. A. Kolpakov, and M. Fridman, Optica **5**, 774 (2018).

[33] B. Li, J. Kang, S. Wang, Y. Yu, P. Feng, and K. K. Y. Wong, Opt. Lett. **44**, 4351 (2019).

[34] Y. Du, Q. Gao, C. Zeng, D. Mao, and J. Zhao, Phys. Rev. A **103**, 063504 (2021).

[35] A. Zaviyalov, O. Egorov, R. Iliew, and F. Lederer, Phys. Rev. A **85**, 013828 (2012).

[36] J. P. Lauterio-Cruz, H. E. Ibarra-Villalon, O. Pottiez, Y. E. Bracamontes-Rodriguez, O. S. Torres-Munoz, J. C. Hernandez-Garcia, and H. Rostro-Gonzalez, Opt. Express **27**, 37196 (2019).

[37] K. Goda and B. Jalali, Nat. Photonics **7**, 102 (2013).

[38] A. Mahjoubfar, D. V. Churkin, S. Barland, N. Broderick, S. K. Turitsyn, and B. Jalali, Nat. Photonics **11**, 341 (2017).

[39] G. Herink, B. Jalali, C. Ropers, and D. R. Solli, Nat. Photonics **10**, 321 (2016).

[40] S. D. Chowdhury, B. D. Gupta, S. Chatterjee, R. Sen, and M. Pal, Opt. Lett. **44**, 2161 (2019).

[41] M. Liu, T. J. Li, A. P. Luo, W. C. Xu, and Z. C. Luo, Photonics Res. **8**, 246 (2020).

[42] Y. Zhou, Y. X. Ren, J. Shi, and K. K. Y. Wong, Photonics Res. **8**, 1566 (2020).

[43] Z. Liu, S. Zhang, and F. W. Wise, Opt. Lett. **40**, 1366 (2015).

[44] C. Lecaplain and P. Grelu, Phys. Rev. A **90**, 013805 (2014).

[45] F. Meng, C. Lapre, C. Billet, T. Sylvestre, J. M. Merolla, C. Finot, S. K. Turitsyn, G. Genty, and J. M. Dudley, Nat. Commun. **12**, 5567 (2021).

[46] B. Redding, A. Cerjan, X. Huang, M. L. Lee, A. D. Stone, M. A. Choma, and H. Cao, Proc. Nat. Acad. Sci. USA **112**, 1304 (2015).

[47] Y. Bromberg, Y. Lahini, E. Small, and Y. Silberberg, Nat. Photonics **4**, 721 (2010).

[48] K. Kim, S. Bittner, Y. Zeng, S. Guazzotti, O. Hess, Q. J. Wang, and H. Cao, Science **371**, 948 (2021).

[49] A. Argyris, D. Syvridis, L. Larger, V. Annovazzi-Lodi, P. Colet, I. Fischer, J. García-Ojalvo, C. R. Mirasso, L. Pesquera, and K. A. Shore, Nature (London) **438**, 343 (2005).

[50] Y. Du, S. V. Sergeyev, Z. Xu, M. Han, X. Shu, and S. K. Turitsyn, Laser Photonics Rev. **14**, 1900219 (2020).

[51] J. F. Kenney, *Mathematics of Statistics*, 2nd ed. (D. Van Nostrand, New York, 1939).

[52] Y. S. Kivshar and B. A. Malomed, Rev. Mod. Phys. **61**, 763 (1989).

[53] Y. S. Kivshar, IEEE J. Quantum Electron. **29**, 250 (1993).

[54] G. P. Agrawal, *Nonlinear Fiber Optics* (Springer, Berlin, Heidelberg, 2000).

[55] S. A. Planas, N. L. Pires Mansur, C. H. Brito Cruz, and H. L. Fragnito, Opt. Lett. **18**, 699 (1993).

[56] Y. Du, C. Zeng, Z. He, Q. Gao, D. Mao, and J. Zhao, Phys. Rev. A **104**, 023503 (2021).

[57] See Supplemental Material at http://link.aps.org/supplemental/10.1103/PhysRevA.106.053509 for this movie shows the intra-cavity evolution of the temporal profile, spectrum, and two-dimensional time-frequency spectrogram of the noise-like pulse in the single-mode fiber in the roundtrip where the spectral rogue wave occurs.

[58] D. Mao, Z. He, Q. Gao, C. Zeng, L. Yun, Y. Du, H. Lu, Z. Sun, and J. Zhao, Ultrafast Science **4**, 9760631 (2022).

[59] J. P. Lourdesamy, A. F. J. Runge, T. J. Alexander, D. D. Hudson, A. Blanco-Redondo, and C. M. de Sterke, Nat. Phys. **18**, 59 (2021).

[60] D. Mao, H. Wang, H. Zhang, C. Zeng, Y. Du, Z. He, Z. Sun, and J. Zhao, Nat. Commun. **12**, 6712 (2021).

[61] O. Pottiez, J. P. Lauterio-Cruz, Y. E. Bracamontes-Rodriguez, H. E. Ibarra-Villalon, J. C. Hernandez-Garcia, M. Bello-Jimenez, and E. A. Kuzin, Opt. Express **27**, 34742 (2019).